Nanoscale

ROYAL SOCIETY OF CHEMISTRY

PAPER

View Article Online
View Journal | View Issue

Cite this: *Nanoscale*, 2020, **12**, 22817

Experimental signature of a topological quantum dot

Marie S. Rider,*[a] Maria Sokolikova,[b] Stephen M. Hanham,[b,c] Miguel Navarro-Cía,[d] Peter D. Haynes,[b] Derek K. K. Lee,[a] Maddalena Daniele,[e] Mariangela Cestelli Guidi,[f] Cecilia Mattevi,[b] Stefano Lupi[e] and Vincenzo Giannini[g]

Received 9th September 2020,
Accepted 1st November 2020

DOI: 10.1039/d0nr06523d

rsc.li/nanoscale

Topological insulator nanoparticles (TINPs) host topologically protected Dirac surface states, just like their bulk counterparts. For TINPs of radius <100 nm, quantum confinement on the surface results in the discretization of the Dirac cone. This system of discrete energy levels is referred to as a topological quantum dot (TQD) with energy level spacing on the order of Terahertz (THz), which is tunable with material-type and particle size. The presence of these discretized energy levels in turn leads to a new electron-mediated phonon-light coupling in the THz range, and the resulting mode can be observed in the absorption cross-section of the TINPs. We present the first experimental evidence of this new quantum phenomenon in Bi_2Te_3 topological quantum dots, remarkably observed at room temperature.

Topological nanophotonics is an emerging discipline that aims to control light at the nanoscale using topological states.[1] Topological insulator nanoparticles (TINPs) provide an excellent route towards this goal, and so understanding and experimentally demonstrating how they interact with light is of paramount importance.

Topological insulators (TIs) are 3D materials which are insulating in the bulk but host topologically protected, conducting surface states.[2–5] These surface states display a linear dispersion relation, seen as a Dirac cone which bridges the bulk band gap. The Dirac cone can only be opened by breaking time-reversal symmetry, making these states remarkably robust to perturbations such as material defects and stray (non-magnetic) fields. These surface states also do not exhibit back scattering.

In a bulk sample, only a small number of atoms in the material contribute to surface state behaviour and so topological effects are notoriously weak. Nanoscale structures have an enhanced surface area to bulk ratio, and a larger proportion of atoms participate in the surface physics. This results in a pronounced topological contribution to the electronic and optical properties of the system. Pioneering theoretical work[6,7] has studied spherical topological insulator particles. Spherical TINPs have a maximal surface to volume ratio whilst still maintaining a true 3D 'bulk'. These finite systems exhibit the same level of topological protection as their continuous counterparts,[8] but quantum confinement results in the discretization of the surface state energies, with energy spacing on the order of Terahertz (THz). This has exciting implications for both the electronic and optical properties of the nanostructures[9–14] and recent theoretical work has also studied the optical properties of hybrid systems coupling the energy levels of TINPs with quantum dots and emitters.[15,16] The THz regime (~0.1–10 THz) is notoriously difficult to access with plasmonic or purely photonic technologies, so investigation of TINPs and their hybrid systems could lead to important advancements in the development of THz sensors, lasers and waveguides.[1,17,18]

Some nanostructures (such as nanoribbons and thin films[19]) can already be reliably produced, but equiaxed (*e.g.* spherical or rhombohedral) TINPs have so far proved technically challenging.[20,21] This means that their optical properties have received relatively little experimental attention. The identification and classification of modes in the optical spectra of other TI nanostructure samples (such as nanosheets and nanoplates) has been a lively endeavour, oftentimes leading to contradictory conclusions.[22–28] Unexpected peaks observed with Raman and optical spectroscopy have been attributed to multiple different origins, such as surface oxi-

[a]*The Blackett Laboratory, Imperial College London, London SW7 2AZ, UK. E-mail: marie.rider@ic.ac.uk*
[b]*Department of Materials, Imperial College London, London SW7 2AZ, UK*
[c]*Department of Electronic, Electrical and Systems Engineering, University of Birmingham, Birmingham B15 2TT, UK*
[d]*School of Physics and Astronomy, University of Birmingham, Birmingham B15 2TT, UK*
[e]*INFN and Department of Physics, Sapienza University of Rome, Piazzale A. Moro 2, 00185 Rome, Italy*
[f]*INFN-LNF, Via Enrico Fermi 40, 00444 Frascati (Roma), Italy*
[g]*Instituto de Estructura de la Materia (IEM-CSIC), Consejo Superior de Investigaciones Científicas, Serrano 121, 28006 Madrid, Spain. http://www.GianniniLab.com*

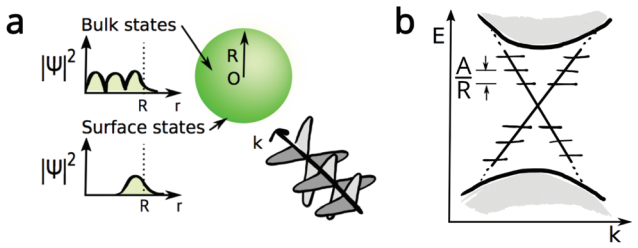

Fig. 1 Small topological insulator nanoparticles: (a) Schematic of TINP of radius R irradiated with light, illustrating bulk states and surface states which decay into the bulk with a length scale ~Å. (b) For small TINPs (R < 100 nm) the Dirac cone becomes discretized with the position of energy levels inversely scaling with R.

dation, phonon confinement effects, unverified topological effects or simply left unclassified. The presence of discretized energy levels in TINPs leads to a new electron-mediated phonon–light coupling in the Terahertz (THz) range. This work presents evidence of a new, purely topological contribution to the spectra of TINPs.

In the case of small ($5 < R/\text{nm} < 100$) TINPs the continuous Dirac cone becomes discretized due to finite size effects, giving a set of discrete energy levels much like those in a quantum dot.[12,13] A schematic of a spherical TINP and its bulk and surface states is given in Fig. 1a. These energy levels are equally spaced, with energies increasing away from the Γ-point in integer values of A/R (as illustrated schematically in Fig. 1b). A = 2.0 eV Å is a material-dependent quantity, given by the matrix element of momentum calculated for a four band model Hamiltonian of Bi_2Te_3 and averaged over three axes, calculated by a density functional theory approach and taken from Liu *et al.*,[29] discussed in more detail in Appendix A. When irradiated with THz (1 THz = 33 cm^{-1} = 4 meV) light, a transition between two of these topological, delocalised surface states occurs within the same frequency range as a bulk phonon excitation, resulting in a strong Fano resonance, referred to as the surface topological particle (SToP) mode.[12] This is a purely quantum mechanical feature of the system, and the asymmetric profile of this resonance creates a point of zero-absorption when the energy spacing of the surface states is matched by the incident light. This means that the excitation of a single electron occupying a topological surface state can shield the bulk from the absorption of incoming light. This mode has been theoretically predicted but had not been experimentally observed until the present work. Light–matter interactions in nanoparticles requiring a quantum mechanical approach have attracted much attention in quantum plasmonics in recent years,[30] and TINPs made of materials such as Bi_2Te_3 present a promising extension of this field.

Bismuth telluride nanoparticle synthesis

Bi_2Te_3 has a layered crystal structure with quintuple covalently-bonded Te–Bi–Te–Bi–Te layers stacked along the c-axis and therefore can be easily produced in the form of two-dimensional sheets *via* physical[31] or wet-chemical methods.[32] In order to suppress preferential formation of anisotropic two-dimensional structures unavoidable in the direct solution-phase synthesis due to the high reactivity of Bi salts, spherical Bi_2Te_3 nanoparticles were synthesised using a two-stage reaction analogously to ref. 20. Briefly, the growth involved the reduction of Bi ions by organic primary amine in an inert atmosphere leading to the formation of spherical Bi nanoparticles and followed by tellurisation of the produced Bi nanospheres in trioctylphosphine telluride solution. Transmission electron microscopy (TEM) images shown in Fig. 2a and b are representative images of the ensembles of Bi and Bi_2Te_3 nanoparticles respectively. The Bi nanoparticles are nearly spherical with radius of 14.4 ± 2.3 nm, while upon tellurisation the shape of Bi_2Te_3 nanoparticles changes to slightly rhombohedral with a larger average radius of 17.5 nm (standard deviation 1.8 nm) due to the inclusion of tellurium

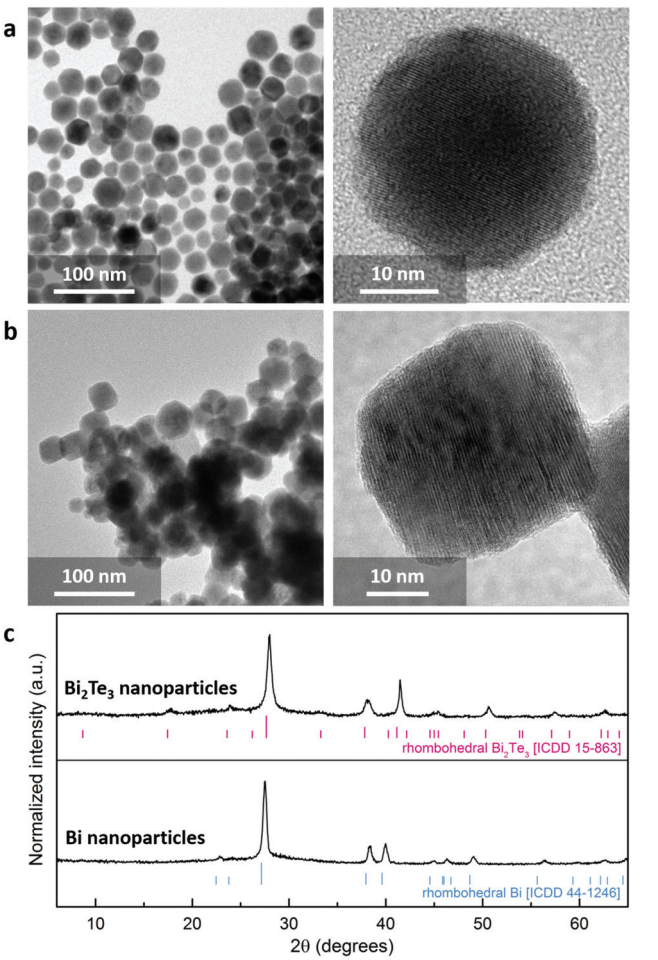

Fig. 2 Bi_2Te_3 nanoparticle synthesis: (a) TEM images of Bi nanoparticles, which are nearly spherical and of average radius 14.4 nm. (b) Successfully synthesized Bi_2Te_3 nanoparticles with a slightly rhombohedral shape and average radius of 17.5 nm. (c) X-ray diffraction patterns illustrating the successful tellurisation of the Bi nanoparticles to form Bi_2Te_3 nanoparticles.

species. Powder X-ray diffraction (XRD) patterns of both intermediate Bi and final Bi_2Te_3 nanoparticles clearly demonstrate a phase change accompanied by a significant shift of the diffraction peaks to the higher angles corresponding to smaller interplanar distances of the rhombohedral Bi_2Te_3 lattice (Fig. 2c). A more detailed experimental method is provided in Appendix B.

Theoretical framework

In the theoretical treatment of a TINP irradiated with THz light of frequency ν, we treat the bulk behaviour classically with a bulk dielectric function and the surface states are treated quantum mechanically. We focus on Bi_2Te_3 but the following analytic results are valid for other materials within the Bi_2Te_3 family given the correct parameter substitutions. We follow the theory method given in ref. 12. We work in the limit in which the particle radius R is much smaller than the wavelength of incoming light, $R \ll \lambda$. The bulk dielectric function of Bi_2Te_3 is a rank 2 tensor and to treat the system analytically we take $\varepsilon(\nu)$ as a diagonal matrix with principal components $[\varepsilon_\perp(\nu), \varepsilon_\perp(\nu), \varepsilon_\parallel(\nu)]$ and all other components equal to 0. $\varepsilon_\parallel(\nu)$ gives the dielectric function along the c-axis of the material, while $\varepsilon_\perp(\nu)$ is the dielectric function in both axes perpendicular to the c-axis. Here, we assume that each component can be described through a Lorentzian shape

$$\varepsilon(\nu) = \sum_{j=\alpha,\beta,f} \frac{{\nu_{p,j}}^2}{{\nu_{0,j}}^2 - \nu^2 - i\gamma_j\nu}, \quad (1)$$

which contains contributions from α and β transverse phonons and free charge carriers (denoted by f) arising from bulk defects. In this last case, $\nu_{0,j} = 0$. $\nu_{p,j}$, $\nu_{0,j}$ and γ_j denote the amplitude, resonance frequency and harmonic broadening parameters for each mode. The parameters (given in Table 1) for $\varepsilon_\parallel(\nu)$ have been determined by fitting to experimental data for samples illuminated with light propagating along the c-axis of the material,[33] and measured at 300 K. The real and imaginary parts of $\varepsilon_\parallel(\nu)$ are plotted in Fig. 3a with purple and green lines respectively. To present a transparent analysis, the following theoretical study only considers the contribution to the TINP optical response from $\varepsilon_\parallel(\nu)$. We also expect a contribution from $\varepsilon_\perp(\nu)$ (and so should average over all three material axes), but due to limited reliable $\varepsilon_\perp(\nu)$ data, we present theoretical results derived using only $\varepsilon_\parallel(\nu)$. Considering the material isotropic in this manner does not affect the conclusions of this work. However for reference, the plot of $\varepsilon_\parallel(\nu)$ in Fig. 3a is annotated with vertical lines denoting the α and β phonon frequencies for both $\varepsilon_\parallel(\nu)$ and $\varepsilon_\perp(\nu)$ (values taken from ref. 34). For $\varepsilon_\parallel(\nu)$, the resonance frequencies for the α and β phonons are 1.56 THz and 2.85 THz respectively (as given in Table 1), whilst for $\varepsilon_\perp(\nu)$, the frequencies used are 2.82 THz and 3.60 THz respectively.

Table 1 Parameters of $\varepsilon_\parallel(\nu)$ for Bi_2Te_3 (extracted from experimental data in ref. 33). $\nu_{p,j}$, $\nu_{0,j}$ and γ_j denote the amplitude, resonance frequency and harmonic broadening parameters for each mode

	$\nu_{p,j}$ (THZ)	$\nu_{0,j}$ (THZ)	γ_j (THZ)
α	21	1.56	0.18
β	4	2.85	0.2
f	11	0	0.24

The absorption cross-section for a spherical particle suspended in a transparent material (in our case, mineral oil in order to preserve the quality of the particles, for which n_{oil} = 1.47 and $\varepsilon_{oil} = {n_{oil}}^2$ = 2.16, (ref. 35) is calculated from the imaginary component of the particle polarizability α_0, such that $\sigma_{abs} = \frac{k}{\varepsilon_0}\mathrm{Im}\{\alpha_0\}$ and is given by

$$\sigma_{abs}(\nu) = 4\pi R^3 n_{oil}\frac{2\pi}{\lambda}\mathrm{Im}\left[\frac{\varepsilon(\nu) + \delta_R(\nu) - \varepsilon_{oil}}{\varepsilon(\nu) + \delta_R(\nu) + 2\varepsilon_{oil}}\right], \quad (2)$$

and for a Fermi level which resides in the band gap between energy levels separated by energy A/R, the δ_R contribution is given by

$$\delta_R(\nu) = \frac{e^2}{3\pi\varepsilon_0}\left(\frac{1}{A - h\nu R} + \frac{1}{A + h\nu R}\right). \quad (3)$$

δ_R is the contribution to the particle polarizability from the topological delocalised surface states, in which transitions occur between the quantized energy levels of the discretized Dirac cone resulting in a modified surface charge density. The derivation of this term can be found in the ESI of ref. 12. For a Fermi level within $\pm A/R$, δ_R is modified (for more details see Appendix C) owing to the absence of an energy level at the Dirac point. While we do not know the precise Fermi level of each TINP in the experimental sample, Bi_2Te_3 samples tend to be n-doped, resulting in the Fermi level residing close to or in the conduction band. It is thus assumed that very few TINPs in the sample will contribute a topological term to the absorption cross-section, and those which do contribute will likely not have a Fermi level close to the Dirac point. In the absence of surface states (such as by applying a magnetic field term and thus destroying the surface states), $\delta_R = 0$ and we return to the usual solution of a dielectric sphere in a constant electric field.

For a given Fermi level, δ_R varies only with R and ν. In Fig. 3b, we plot the theoretically expected absorption cross-sections of TINPs with $E_F = A/R$ and radii 15, 20 and 25 nm respectively, and the topologically trivial case where $\delta_R = 0$. Each cross-section with a topological contribution has a characteristic shape of three peaks, corresponding to the β phonon mode, a localised surface plasmon-polariton (LSPP) mode, and the SToP mode. A point of zero absorption can be seen for each SToP mode, at which a single electron in a Dirac state shields the bulk from absorbing incoming light. The LSPP and β modes are bulk contributions and as such, their positions do not change with particle size. The SToP peak position and point of zero-absorption do vary with R. As the particle size varies, the spacing between discretized surface state energies varies as $\sim 1/R$. This in turn changes the frequency at

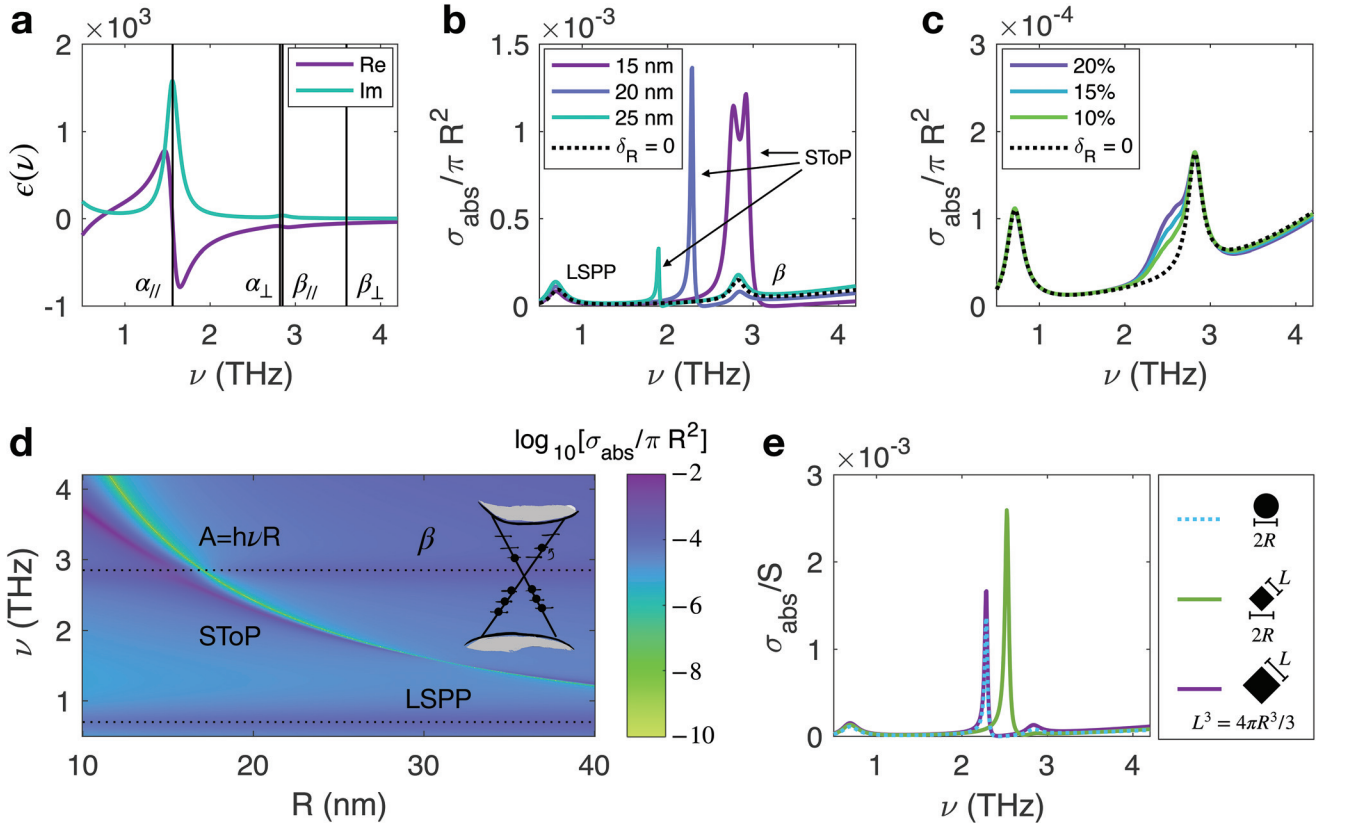

Fig. 3 Theoretical SToP results: (a) The real (purple) and imaginary (green) components of Bi_2Te_3 bulk dielectric function $\varepsilon_{\|}(\nu)$, for incident light parallel to the c-axis using parameters fitted to data in ref. 33, presented in Table 1. The positions of the α and β phonon frequencies are annotated for both $\mathbf{k}\|c$-axis and $\mathbf{k}\perp c$-axis incoming light (denoted $\alpha_{\|}$, $\beta_{\|}$, $\alpha_{\perp}$, and $\beta_{\perp}$ respectively). (b) Absorption cross-section of a TINP with $E_F = A/R$, R = (15, 20, 25) nm and a TINP of radius 15 nm for which $\delta_R = 0$. The LSPP and β mode are visible and labelled, whilst the α mode is over-damped and thus not seen in the theoretically calculated absorption cross-section. Increased TINP radius results in a lower frequency SToP mode peak (also labelled). For R = 15 nm, the SToP mode and β modes overlap and a split peak is seen. For each SToP mode there is a point of zero absorption which occurs to the right of the peak. (c) For an ensemble of particles with a Gaussian distribution of radii ($\bar{R}$ = 17.5 nm and standard deviation 1.8 nm) and in which only (10, 15, 20)% of TINPs show a SToP mode, the peak height is reduced and no longer displays a point of zero absorption. (d) Absorption cross-section varying with R and ν. The bulk LSPP and β phonon positions remain constant for varying radius size, and the line of zero-absorption is annotated ($A = h\nu R$). (e) Comparison of absorption cross-section for nanoparticles of varying geometry and size. Absorption cross-section of sphere (dotted blue) with R = 20 nm, projection $S = \pi R^2$. Absorption cross-section for a cube with diagonal length $2R$ = 40 nm (green), such that L = 28.2 nm, and projection $S = L^2$. Absorption cross-section of cube of length L = 32.2 nm (purple) and $S = L^2$, with volume $V = L = 4\pi R_{\text{eff}}^3/3$ such that effective radius R_{eff} = 20 nm.

which the particle polarizability is modified when a surface state is excited, as described by $\delta_R(\nu)$ in eqn (3). This in turn leads to a R-dependence of the absorption cross-section of the nanoparticle. As particle size is reduced, the frequency of surface state excitations increases, and thus the SToP mode peak and point of zero-absorption both shift to higher frequencies. For particles of approximately R = 15 nm, the SToP mode appears on top of the β phonon mode, resulting in a double peak structure of broader linewidth. The R and ν dependence of the absorption cross-section is illustrated in Fig. 3d. A study of how the absorption cross-section is modified by isolating the various phonon contributions in the dielectric function is given in the Appendix D.

The synthesised Bi_2Te_3 nanoparticles discussed in this work are rhombohedral, however their topological properties are well-approximated by those of spherical particles, due to the robustness of topological states against surface deformation. This is demonstrated in ref. 6 and 12 in which it is shown that the discrete energy levels of TI spheres and cubes of equal volume converge for particles of radius $R > 10$ nm. This means that the topological contribution to the absorption cross-section is also the same for particles of equal volume. If a cube of volume V were to be deformed to a sphere, it would have an effective radius R_{eff}, such that $V = 4\pi R_{\text{eff}}^3/3$. This value of R_{eff} can then be used in eqn (3) to calculate the topological contribution to the absorption cross-section, δ_R. The absorption cross-section of a cube can be calculated analytically,[36] with the topological contribution described as above. In Fig. 3e we plot the absorption cross-sections of a sphere with R = 20 nm (dotted blue), a cube with diagonal length $2R$ (green), such that L = 28.3 nm and cube with R_{eff} = 20 nm (purple), such that it has the same volume as the sphere. The cross-sec-

tions are normalised by the projection of each nanostructure, *i.e.* $S = \pi R^2$ for the sphere and $S = L^2$ for the cubes. The qualitative results for each nanostructure are very similar, with the sphere and cube of equal volume demonstrating a SToP peak and point of zero-absorption at the same position. The cube with diagonal length equal to the diameter of the sphere has a slightly smaller effective radius, and thus presents a SToP mode and point of zero-absorption shifted to a slightly higher frequency. As the rhombohedral nanoparticles in our experiment fall between the two limits of a sphere and a cube, we conclude that approximating the rhombohedral nanoparticles as spherical should give a qualitatively good result.

So far we have discussed the optical properties of a single TINP, which is representative of an ensemble of non-interacting particles of equal radius, normalised to the number of TINPs. However in our experimental sample, we have a partial agglomerate of nanoparticles, and the nanoparticles have a range of radii. Before measurements were taken, the sample was agitated to separate the nanoparticles. It is however inevitable that some particles will remain as an agglomerate. We would expect this agglomerate to contribute to the bulk properties of the absorption-cross section, but lose the quantum confinement effects expected from small, separate nanoparticles. Any topological peak from such a large mass of material would occur at such a low frequency as to not be measured in our experiment. For example, a particle of R = 100 nm would be expected to exhibit a SToP mode peak at approximately 0.45 THz with a greatly suppressed amplitude. This is outside of the frequency range of our measured data. Due to uncertainty in the Fermi level and orientation of each TINP in relation to the incoming light, it can be assumed that while all TINPs contribute to the bulk properties of the absorption cross-section, only a small percentage will give a topological contribution. Fig. 3c illustrates the theoretically calculated absorption cross-section of an ensemble of TINPs of mean radius 17.5 nm and standard deviation 1.8 nm (values taken from analysis of TEM images of the experimental sample), with a varying percentage contributing to the topological property. The peak height is greatly suppressed and a point of zero-absorption is no longer observed.

Results

In Fig. 4, we show the experimental absorption cross-section (solid black line) of Bi_2Te_3 TINPs suspended in mineral oil, measured at 300 K. The vertical dotted lines denote the four phonon frequencies ($\alpha_\parallel$, $\beta_\parallel$, $\alpha_\perp$, $\beta_\perp$) corresponding to the two bulk dielectric functions $\varepsilon_\parallel$ and $\varepsilon_\perp$ respectively. We have performed a Lorentzian decomposition using four Lorentz peaks, with fit values given in Table 2. Using four peaks (which we label P1–P4) yields a fitting error of 0.23%, whereas using three or five peaks results in an error of 2.3% or 3.4% respectively. We assign P3 and P4 to the $\beta_\parallel$ and $\beta_\perp$ phonons respectively. α phonons are typically under-damped in bulk samples and so not observed in the theoretical calculations of the

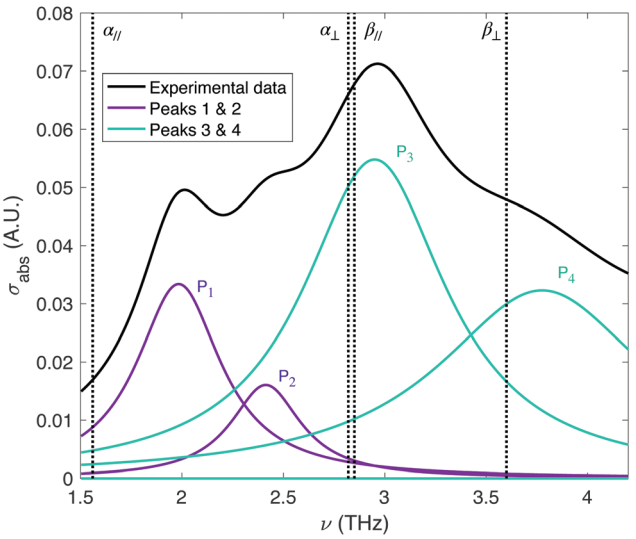

Fig. 4 Experimental results: Experimental absorption cross-section data with impurity absorption band subtracted, superimposed with a Lorentzian decomposition of the same data, fitted with four peaks, P1–P4. This data was taken from a sample of Bi_2Te_3 nanoparticles with $\bar{R}$ = 17.5 nm and standard deviation 1.8 nm.

Table 2 Parameters of four peak Lorentzian fit with a fit error of 0.24%

	P1	P2	P3	P4
Peak position (THz)	1.98	2.41	2.95	3.77
Peak width (THz)	0.51	0.42	0.86	1.26

absorption cross-section using the bulk dielectric function (as demonstrated in Fig. 3b and c). This can be understood by studying the bulk dielectric function for Bi_2Te_3 depicted in Fig. 3a, where the very large value of $\mathrm{Im}[\varepsilon(\nu)]$ at the α phonon frequency will result in a very small contribution to σ_{abs} (given in eqn (2)) at this frequency. However, finite size effects may reduce damping of transverse modes, resulting in an increased amplitude which may be visible in the absorption cross-section. So, it is possible that the $\alpha_\perp$ phonon also slightly contributes to the amplitude of P3.

P1 and P2 do not appear to relate to any expected bulk modes. We rule out oxidation effects as the sample was kept in chloroform, and exchanged for mineral oil for THz measurements. Samples typically show oxidation effects on the timescale of days,[25] which is not the case for our sample. We note that P2 appears at a frequency commensurate with the SToP mode peak predicted for an ensemble of varying radius as demonstrated in Fig. 3c. While the short height of the SToP mode peak is partially explained by the assumption that very few particles contribute to the topological properties of the sample, we also note that our theory is modelled at zero temperature, whereas the experiment operates at room temperature (~6 THz), where the probability of finding a level empty in our system is low. Temperature smearing will result in the modes

seen experimentally being less visible than those seen in theory. This could be remedied by studying a TI with a bigger band gap and/or smaller particles. It is possible that the presence of two new non-bulk modes (P1 and P2) is due to SToP modes resulting from both the $\alpha_{\parallel}$ and $\alpha_{\perp}$ phonons.

The observation of two unexpected peaks at frequencies which do not relate to expected bulk modes allows us to conclude that at least one of the peaks is likely topological in origin. We conclude from this experimental comparison with the theory model that we have observed the SToP mode in Bi_2Te_3 nanoparticles, which was theoretically predicted in ref. 12.

Author contributions

V.G. and M.S.R. proposed the initial idea. M.S. and C.M. synthesized the nanoparticles and performed the X-ray characterization. S.L., M.C.G., and M.D performed the THz measurements. S.M.H. and M.N.-C. together with M.S. and C.M. worked on how to stabilize the nanoparticles in oil. S.M.H. and M.N.-C. also performed some initial THz measurement. P.D.H., D.L., V.G., and M.S.R. discussed the theoretical model as well as the numerical implementation. M.S.R. performed the simulations and wrote the first draft. All authors discussed the results and contributed to the manuscript. V.G. supervised the project.

Appendix A: Four band model Hamiltonian

The important topological physics occurs near the Γ-point, allowing us to use **k**·**p** perturbation theory to expand about the Γ-point and write down a low-energy, 4-band effective Hamiltonian,

$$H(\mathbf{k}) = E_0(\mathbf{k})\mathbf{1}_4 + \begin{pmatrix} \mathcal{M}(\mathbf{k}) & A_1 k_z & 0 & A_2 k_- \\ A_1 k_z & -\mathcal{M}(\mathbf{k}) & A_2 k_- & 0 \\ 0 & A_2 k_+ & \mathcal{M}(\mathbf{k}) & -A_1 k_z \\ A_2 k_+ & 0 & -A_1 k_z & -\mathcal{M}(\mathbf{k}) \end{pmatrix} \quad (4)$$

where $k_{\pm} = k_x \pm \mathrm{i}k_y$, $E_0(\mathbf{k}) = C + D_1 {k_z}^2 + D_2 {k_{\perp}}^2$ and $\mathcal{M}(\mathbf{k}) = M - B_1 {k_z}^2 - B_2 {k_{\perp}}^2$. The parameters ($A_1$, A_2, B_1, B_2, C, D_1, D_2, M) in this effective model can be determined by fitting the energy spectrum of the Hamiltonian to that of *ab initio* calculations,[37] with the results for $Bi_2(Se_xTe_{1-x})_3$ presented by Liu *et al.*[29] In the theory model used in this work, the crystal structure is taken to be isotropic, such that $A = \frac{1}{3}(A_1 + 2A_2)$. Fig. 5a shows how the theoretically calculated absorption cross-section varies with uncertainty in A. Shifting $A \rightarrow A'$ by 10% shifts the position of the SToP peak by <10%. Fig. 5b illustrates that modifying the magnitude of the topological contribution to the particle polarizability $\delta_R(\nu)$ (by multiplying by a constant coefficient δ_{coeff}), has little effect on the position of the SToP peak. Fig. 5c shows that when a finite lifetime of excited surface states is considered (by detracting a small, complex component $\mathrm{i}\Gamma A$ from the denominator of all $\delta_R(\nu)$ terms), the height of the SToP mode peak becomes smaller (for a particle of R = 20 nm and Γ = 0.01, the height of the SToP mode peak reduces by ~45%) and the position remains the same.

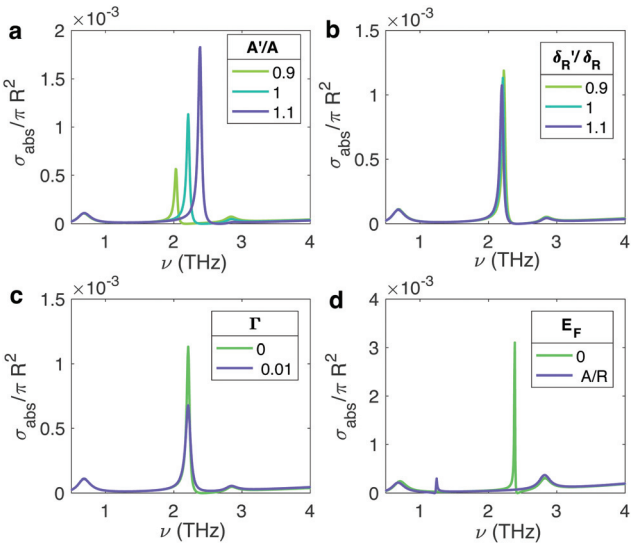

Fig. 5 Modifying theory parameters and Fermi level: (a) For R = 20 nm, varying A by 10%, which shifts the position of the SToP mode peak and modifies the height of the peak. (b) Varying the magnitude of $\delta_R(\nu)$ by 10%, which has no effect on the position of the SToP mode peak and very little effect on the height of the peak. (c) Introducing a small complex component to the denominator of $\delta_R(\nu)$, $\mathrm{i}\Gamma A$, equivalent to introducing a finite life-time to the excited surface states. Introduction of this finite lifetime reduces the height of the SToP mode peak. (d) Changing the Fermi level from $E_F = A/R$ to $E_F = 0$ (for R = 40 nm) results in the SToP mode occurring at twice the frequency of incoming light, shown for R = 40 nm.

Appendix B: Experimental method – further details of synthesis and THz measurements

In a standard synthesis, 114 mg of bismuth acetate (Bi $(CH_3COO)_3$, 99% Aldrich) and 3.5 mL of 1-dodecanethiol (DDT, 98% Aldrich) were mixed in a three-neck flask and heated to 45 °C under vacuum and kept at this temperature until a transparent pale-yellow solution is formed. Then the flask was flashed with nitrogen and heated to 60 °C and 6.5 mL of oleylamine (OlAm, 70%, Aldrich) was quickly added. After 24 hours the as-prepared bismuth nanoparticles were used without any further purification. For tellurisation 0.45 mL of 1 M trioctylphosphine telluride (TOP : Te) was injected at 60 °C into the solution containing bismuth nanoparticles. The reaction mixture was kept at this temperature for 48 hours until complete tellurisation and then annealed at 110 °C for 8 hours in order to restore crystallinity. Thus produced Bi_2Te_3 nanoparticles were washed three times with ethanol and then redispersed in chloroform. For THz measure-

ments solvent was exchanged to mineral oil. THz measurements were been performed in transmission through a Vertex 70 V Bruker interferometer equipped with a Hg THz source, a Pyroelectric detector and a broad band high resistivity Si beamsplitter.

Appendix C: Modifying the Fermi level

For $-A/R < E_F < A/R$, the dominant transition is between energy levels directly below and above the Fermi-level, of energy $2A/R$.

$$\delta_R(\nu) = \frac{e^2}{6\pi\varepsilon_0}\left(\frac{1}{2A - h\nu R} + \frac{1}{2A + h\nu R}\right). \quad (5)$$

Fig. 5d shows $\sigma_{abs}/\pi R^2$ for a particle R = 40 nm, at the two Fermi levels $E_F = A/R$ and $E_F = 0$. While the bulk modes remain in the same positions, we see a shift in the SToP mode peaks. The behaviour of the SToP mode and zero absorption trough can be seen in Fig. 3e. Although we do not know the precise Fermi level of each TINP in the sample, for particles whose Fermi level resides in the band gap (and thus contribute to the SToP mode peak in the absorption cross-section) it is most likely that transitions are occurring between energy levels separated by A/R rather than $2A/R$.

Appendix D: Modifying theory parameters

The δ_R term in eqn (3) has no dependence on the dielectric function of either the topological material or the mineral oil, but is affected by the A value. The peak in absorption due to the topological term will experience a shift dependent on which material is being used. For example, the SToP peak for a R = 20 nm TINP made of Bi_2Te_3 and Fermi level $E_F = A/R$ will occur at 2.21 THz, whereas for a Bi_2Se_3 TINP of the same radius (with A = 3.0 eV Å,[29] as studied in the original work by Siroki *et al.*[12]) the peak will occur at 3.1 THz.

In order to demonstrate how the various contributions to the dielectric function manifest in the absorption cross-section, we perform a study in which we artificially remove first the α phonon and then the β phonon contribution from the theoretical calculation. For clarity, Fig. 6a gives the absorption cross-section as a function of ν and R with the LSPP contribution artifically removed (such that $\nu_{p,f} = 0$). The position of the removed mode is given in white, while the β phonon peak, SToP mode and trough of zero absorption can be clearly seen. In Fig. 6b, the α phonon contribution is also removed, (such that $\nu_{p,f} = \nu_{p,\alpha} = 0$. The trough of zero absorption can still be seen, but the SToP mode peak is no longer present. This confirms that the SToP mode is mediated by the α phonon. This is further confirmed in Fig. 6c, in which both the LSPP and β phonon contributions are removed ($\nu_{p,f} = \nu_{p,\beta} = 0$) and the SToP mode is still present.

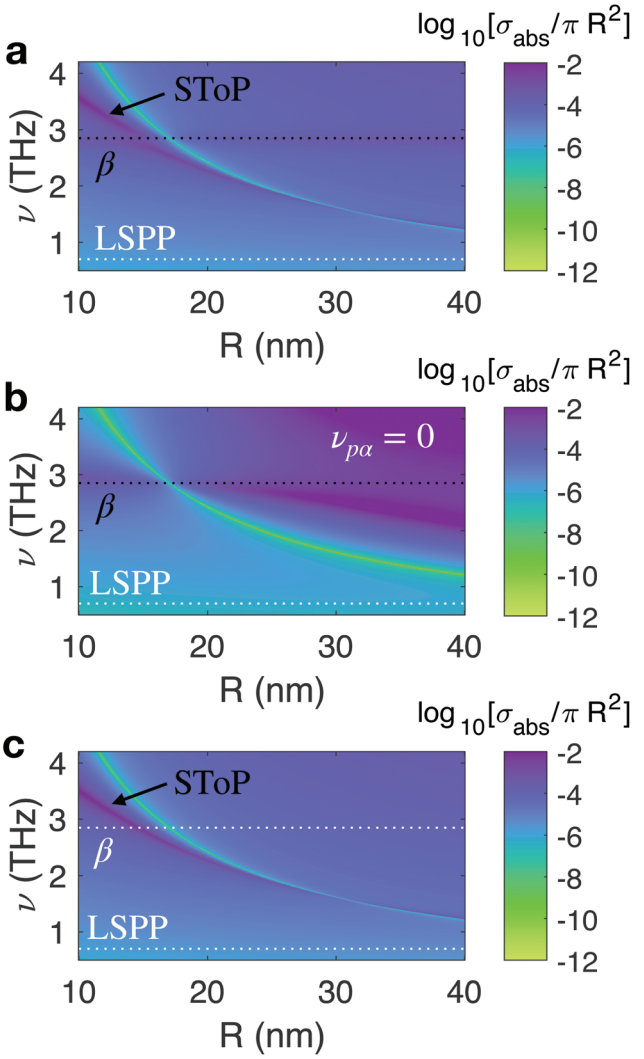

Fig. 6 Modifying the dielectric function: (a) Absorption cross-section with LSPP mode (highlighted with white dotted line) removed from the dielectric function ($\nu_{p,f} = 0$). (b) Absorption cross-section with both LSPP and α phonon contributions removed ($\nu_{p,f} = \nu_{p,\alpha} = 0$). The trough of zero-absorption is still seen, but the SToP mode is no longer present. (c) Absorption cross-section with both LSPP and β phonon contributions (highlighted with a white dotted line) removed ($\nu_{p,f} = \nu_{p,\beta} = 0$).

Conflicts of interest

There are no conflicts to declare.

Acknowledgements

M. S. would like to acknowledge the President's PhD Scholarship programme at Imperial College London for financial support. C. M. would like to acknowledge the EPSRC award EP/M022250/1, and the award of a Royal Society University Research Fellowship by the UK Royal Society. M. S. R. is supported through a studentship in the Centre for Doctoral Training on Theory and Simulation of

Materials at Imperial College London funded by EPSRC Grant No. EP/L015579/1. M. N.-C. acknowledges support from the University of Birmingham (Birmingham Fellowship) and the EPSRC (grant no. EP/S018395/1). V. G. acknowledges the Spanish Ministerio de Economia y Competitividad for financial support through the grant NANOTOPO (FIS2017-91413-EXP), and also the Ministerio de Ciencia, Innovación y Universidades through the grant MELODIA (PGC2018-095777-B-C21).

References

1 M. S. Rider, S. J. Palmer, S. R. Pocock, X. Xiao, P. Arroyo Huidobro and V. Giannini, A perspective on topological nanophotonics: Current status and future challenges, *J. Appl. Phys.*, 2019, **125**(12), 120901.

2 L. Fu, C. L. Kane and E. J. Mele, Topological insulators in three dimensions, *Phys. Rev. Lett.*, 2007, **98**(10), 106803.

3 Y. L. Chen, J. G. Analytis, J.-H. Chu, Z. Liu, S.-K. Mo, X.-L. Qi, H. J. Zhang, D. H. Lu, Xi Dai, Z. Fang, *et al.*, Experimental realization of a three-dimensional topological insulator, Bi_2Te_3, *Science*, 2009, **325**(5937), 178–181.

4 J. E. Moore, The birth of topological insulators, *Nature*, 2010, **464**(7286), 194.

5 T. Stauber, G. Gómez-Santos and L. Brey, Plasmonics in topological insulators: Spin-charge separation, the influence of the inversion layer, and phonon-plasmon coupling, *ACS Photonics*, 2017, **4**(12), 2978–2988.

6 K.-I. Imura, Y. Yoshimura, Y. Takane and T. Fukui, Spherical topological insulator, *Phys. Rev. B: Condens. Matter Mater. Phys.*, 2012, **86**(23), 235119.

7 F. Zhang, C. L. Kane and E. J. Mele, Surface states of topological insulators, *Phys. Rev. B: Condens. Matter Mater. Phys.*, 2012, **86**(8), 081303.

8 G. Siroki, P. D. Haynes, D. K. K. Lee and V. Giannini, Protection of surface states in topological nanoparticles, *Phys. Rev. Mater.*, 2017, **1**, 024201.

9 H.-Z. Lu, W.-Y. Shan, W. Yao, Q. Niu and S.-Q. Shen, Massive Dirac fermions and spin physics in an ultrathin film of topological insulator, *Phys. Rev. B: Condens. Matter Mater. Phys.*, 2010, **81**(11), 115407.

10 H. P. Paudel and M. N. Leuenberger, Three-dimensional topological insulator quantum dot for optically controlled quantum memory and quantum computing, *Phys. Rev. B: Condens. Matter Mater. Phys.*, 2013, **88**(8), 085316.

11 P. Di Pietro, M. Ortolani, O. Limaj, A. Di Gaspare, V. Giliberti, F. Giorgianni, M. Brahlek, N. Bansal, N. Koirala, S. Oh, *et al.*, Observation of Dirac plasmons in a topological insulator, *Nat. Nanotechnol.*, 2013, **8**(8), 556–560.

12 G. Siroki, D. K. K. Lee, P. D. Haynes and V. Giannini, Single-electron induced surface plasmons on a topological nanoparticle, *Nat. Commun.*, 2016, **7**, 12375.

13 L. Gioia, M. Christie, U. Zülicke, M. Governale and A. Sneyd, Spherical topological insulator nanoparticles: Quantum size effects and optical transitions, *Phys. Rev. B: Condens. Matter Mater. Phys.*, 2019, **100**(20), 205417.

14 P. Di Pietro, N. Adhlakha, F. Piccirilli, A. Di Gaspare, J. Moon, S. Oh, S. Di Mitri, S. Spampinati, A. Perucchi and S. Lupi, Terahertz Tuning of Dirac Plasmons in Bi_2Se_3 Topological Insulator, *Phys. Rev. Lett.*, 2020, **124**(22), 226403.

15 G. D. Chatzidakis and V. Yannopapas, Strong electromagnetic coupling in dimers of topological-insulator nanoparticles and quantum emitters, *Phys. Rev. B: Condens. Matter Mater. Phys.*, 2020, **101**, 165410.

16 L. A. Castro-Enriquez, L. F. Quezada and A. Martín-Ruiz, Optical response of a topological-insulator–quantum-dot hybrid interacting with a probe electric field, *Phys. Rev. A*, 2020, **102**, 013720.

17 S. Atakaramians, S. Afshar, T. M. Monro and D. Abbott, Terahertz dielectric waveguides, *Adv. Opt. Photonics*, 2013, **5**(2), 169–215.

18 B. Ferguson and X.-C. Zhang, Materials for terahertz science and technology, *Nat. Mater.*, 2002, **1**(1), 26–33.

19 J. J. Cha, K. J. Koski and Y. Cui, Topological insulator nanostructures, *Phys. Status Solidi RRL*, 2013, **7**(1–2), 15–25.

20 M. Scheele, N. Oeschler, K. Meier, A. Kornowski, C. Klinke and H. Weller, Synthesis and thermoelectric characterization of Bi_2Te_3 nanoparticles, *Adv. Funct. Mater.*, 2009, **19**(21), 3476–3483.

21 M. R. Dirmyer, J. Martin, G. S. Nolas, A. Sen and J. V. Badding, Thermal and electrical conductivity of size-tuned bismuth telluride nanoparticles, *Small*, 2009, **5**(8), 933–937.

22 K. M. F. Shahil, M. Z. Hossain, V. Goyal and A. A. Balandin, Micro-Raman spectroscopy of mechanically exfoliated few-quintuple layers of Bi_2Te_3, Bi_2Se_3, and Sb_2Te_3 materials, *J. Appl. Phys.*, 2012, **111**(5), 054305.

23 O. Caha, A. Dubroka, J. Humlicek, V. Holy, H. Steiner, M. Ul-Hassan, J. Sánchez-Barriga, O. Rader, T. Stanislavchuk, A. Sirenko, *et al.*, Growth, structure, and electronic properties of epitaxial Bismuth Telluride topological insulator films on BaF_2 (111) substrates, *Cryst. Growth Des.*, 2013, **13**(8), 3365–3373.

24 C. Wang, X. Zhu, L. Nilsson, J. Wen, G. Wang, X. Shan, Q. Zhang, S. Zhang, J. Jia and Q. Xue, In situ Raman spectroscopy of topological insulator Bi_2Te_3 films with varying thickness, *Nano Res.*, 2013, **6**(9), 688–692.

25 G. Jian-Hua, Q. Feng, Z. Yun, D. Hui-Yong, H. Gu-Jin, L. Xiao-Nan, Y. Guo-Lin and D. Ning, Surface oxidation properties in a topological insulator Bi_2Te_3 film, *Chin. Phys. Lett.*, 2013, **30**(10), 106801.

26 H. Xu, Y. Song, Q. Gong, W. Pan, X. Wu and S. Wang, Raman spectroscopy of epitaxial topological insulator Bi_2Te_3 thin films on GaN substrates, *Mod. Phys. Lett. B*, 2015, **29**(15), 1550075.

27 X. Qi, W. Ma, X. Zhang and C. Zhang, Raman characterization and transport properties of morphology-dependent two-dimensional Bi_2Te_3 nanofilms, *Appl. Surf. Sci.*, 2018, **457**, 41–48.

28 I. Boulares, G. Shi, E. Kioupakis, P. Lošťák, C. Uher and R. Merlin, Surface phonons in the topological insulators Bi_2Se_3 and Bi_2Te_3, *Solid State Commun.*, 2018, **271**, 1–5.

29 C.-X. Liu, X.-L. Qi, H. Zhang, Xi Dai, Z. Fang and S.-C. Zhang, Model Hamiltonian for topological insulators, *Phys. Rev. B: Condens. Matter Mater. Phys.*, 2010, **82**(4), 045122.

30 J. M. Fitzgerald, P. Narang, R. V. Craster, S. A. Maier and V. Giannini, Quantum plasmonics, *Proc. IEEE*, 2016, **104**(12), 2307–2322.

31 D. Teweldebrhan, V. Goyal and A. A. Balandin, Exfoliation and characterization of Bismuth Telluride atomic quintuples and quasi-two-dimensional crystals, *Nano Lett.*, 2010, **10**(4), 1209–1218.

32 M. S. Sokolikova, P. C. Sherrell, P. Palczynski, V. L. Bemmer and C. Mattevi, Room-temperature growth of colloidal Bi_2Te_3 nanosheets, *Chem. Commun.*, 2017, **53**(57), 8026–8029.

33 A. Dubroka, O. Caha, M. Hronček, P. Friš, M. Orlita, V. Holý, H. Steiner, G. Bauer, G. Springholz and J. Humlíček, Interband absorption edge in the topological insulators $Bi_2(Te_{1-x}Se_x)_3$, *Phys. Rev. B: Condens. Matter Mater. Phys.*, 2017, **96**, 235202.

34 W. Richter and C. R. Becker, A Raman and far-infrared investigation of phonons in the rhombohedral V2–VI3 compounds Bi_2Te_3, Bi_2Se_3, Sb_2Te_3 and $Bi_2(Te_{1-x}Se_x)_3$ ($0 < x < 1$), $(Bi_{1-y}Sb_y)_2Te_3$ ($0 < y < 1$), *Phys. Status Solidi B*, 1977, **84**(2), 619–628.

35 M. Naftaly, *Terahertz metrology*, Artech House, 2015.

36 E. Massa, S. A. Maier and V. Giannini, An analytical approach to light scattering from small cubic and rectangular cuboidal nanoantennas, *New J. Phys.*, 2013, **15**(6), 063013.

37 H. Zhang, C.-X. Liu, X.-L. Qi, Xi Dai, Z. Fang and S.-C. Zhang, Topological insulators in Bi_2Se_3, Bi_2Te_3 and Sb_2Te_3 with a single Dirac cone on the surface, *Nat. Phys.*, 2009, **5**(6), 438.